






In the format provided by the authors and unedited.

High-resolution remote thermometry and thermography using luminescent low-dimensional tin-halide perovskites

Sergii Yakunin ^{1,2*}, Bogdan M. Benin ^{1,2}, Yevhen Shynkarenko ^{1,2}, Olga Nazarenko^{1,2}, Maryna I. Bodnarchuk^{1,2}, Dmitry N. Dirin ^{1,2}, Christoph Hofer³, Stefano Cattaneo³ and Maksym V. Kovalenko ^{1,2*}

¹Laboratory of Inorganic Chemistry, Department of Chemistry and Applied Biosciences, ETH Zurich, Zurich, Switzerland. ²Laboratory for Thin Films and Photovoltaics, Empa – Swiss Federal Laboratories for Materials Science and Technology, Dübendorf, Switzerland. ³Swiss Center for Electronics and Microtechnology (CSEM), Center Landquart, Landquart, Switzerland. *e-mail: yakunins@ethz.ch; mvkovalenko@ethz.ch

Supplementary Information

High-resolution remote thermometry and thermography using luminescent low-dimensional tin-halide perovskites

Sergii Yakunin,^{1,2#} Bogdan M. Benin,^{1,2#} Yevhen Shynkarenko,^{1,2} Olga Nazarenko,^{1,2}
Maryna I. Bodnarchuk,^{1,2} Dmitry N. Dirin,^{1,2} Christoph Hofer,³ Stefano Cattaneo³ and Maksym V.
Kovalenko^{1,2*}*

¹ Laboratory of Inorganic Chemistry, Department of Chemistry and Applied Biosciences, ETH
Zürich, CH-8093 Zürich, Switzerland

² Laboratory for Thin Films and Photovoltaics, Empa – Swiss Federal Laboratories for Materials
Science and Technology, CH-8600 Dübendorf, Switzerland

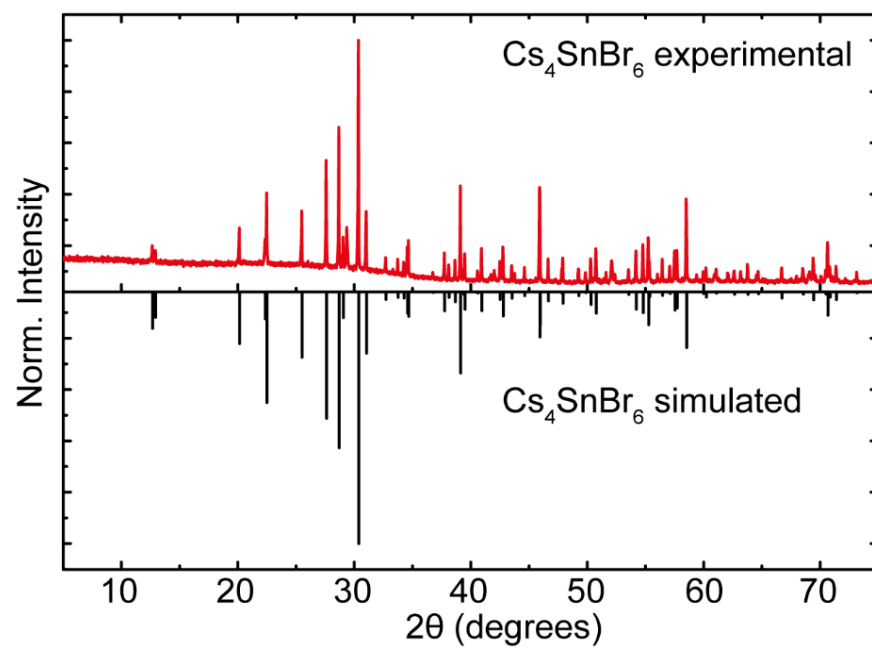
³ Swiss Center for Electronics and Microtechnology (CSEM), Center Landquart, CH-7302
Landquart, Switzerland

Equal contributors. * Corresponding authors.

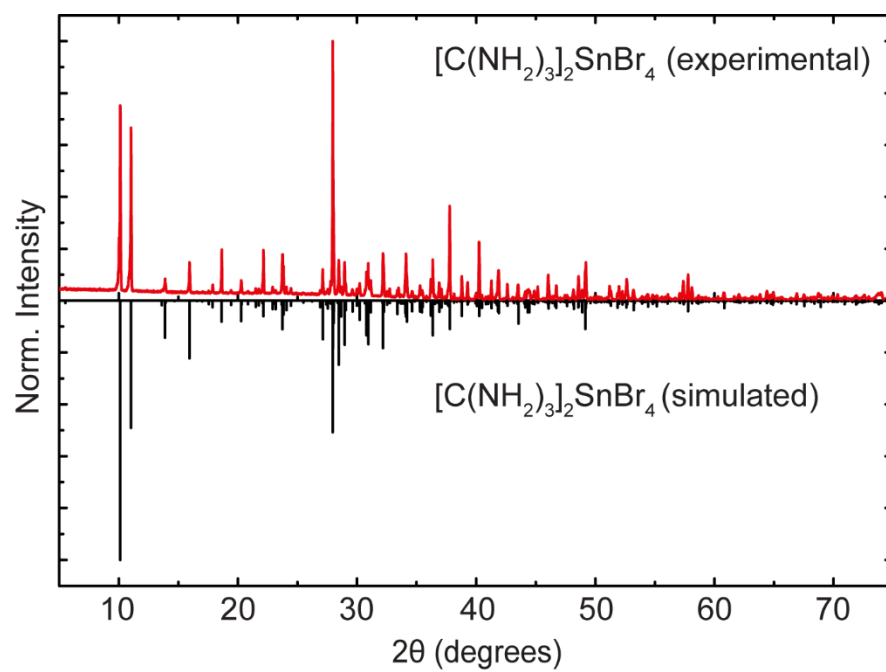
* E-mails: mvkovalenko@ethz.ch; yakunins@ethz.ch

Table of Contents

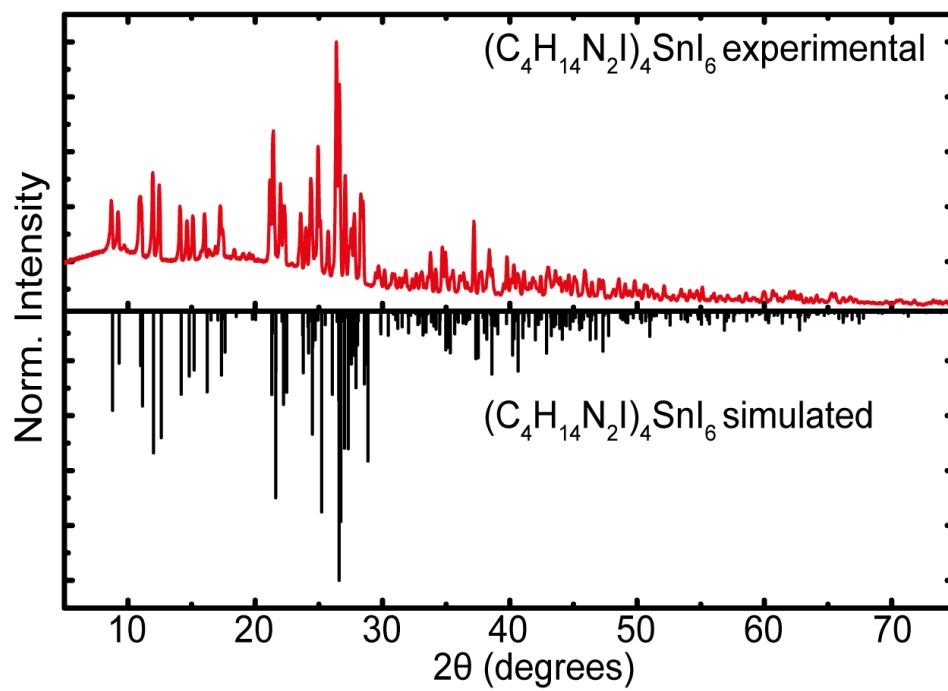
Supplementary Figure 1. Powder X-ray diffraction pattern of Cs_4SnBr_6	3
Supplementary Figure 2. Powder X-ray diffraction pattern of $[\text{C}(\text{NH}_2)_3]_2\text{SnBr}_4$	4
Supplementary Figure 3. Powder X-ray diffraction pattern of $(\text{C}_4\text{H}_{14}\text{N}_2\text{I})_4\text{SnI}_6$	5
Supplementary Figure 4. Optical characterization of $(\text{C}_4\text{N}_2\text{H}_{14}\text{Br})_4\text{SnBr}_6$	6
Supplementary Figure 5. Temperature dependence of Cs_4SnBr_6 PL emission lifetime and intensity.	7
Supplementary Figure 6. Reversible thermal quenching for Cs_4SnBr_6 PL emission.	8
Supplementary Figure 7. Excitation induced heating effects	9
Supplementary Figure 8. Spectrally resolved PL emission lifetimes for Cs_4SnBr_6	10
Supplementary Figure 9. Effect of surrounding on time-resolved PL traces for Cs_4SnBr_6	11
Supplementary Figure 10. Time-resolved PL traces for several batches	12
Supplementary Figure 11. Invariance of PL lifetime of $(\text{C}_4\text{N}_2\text{H}_{14}\text{I})_4\text{SnI}_6$ on oxidation	13
Supplementary Figure 12. PL lifetime temperature dependence for $(\text{C}_4\text{N}_2\text{H}_{14}\text{Br})_4\text{SnBr}_6$	14
Supplementary Figure 13. Specific sensitivity	15
Supplementary Note 1. Models for the fitting of PL lifetime vs. temperature dependence.	16
Supplementary Figure 14. Fitting by the Mott model.	18
Supplementary Table 1. Fitting parameters for the Mott model	18
Supplementary Figure 15. Fitting by the Boltzmann-sigmoid model.	19
Supplementary Table 2. Fitting parameters for Boltzmann-sigmoid model	19
Supplementary Figure 16. Fitting by the exciton-phonon scattering model	20
Supplementary Table 3. Fitting parameters for the exciton-phonon scattering model	20
Supplementary Figure 17. Photographs of the depth standard for ToF imaging in Fig.4a.	21
Supplementary Note 2. Basic principles of ToF-FLI.	22
Supplementary Figure 18. Scheme describing optical ToF measurements	23
Supplementary Note 3. Frequency domain PL lifetime measurement by phase-shift	24
Supplementary Figure 19. Compact stand-alone ToF-FLI prototype	25
Supplementary Note 4. Key specifications of ToF-FLI image sensor used in the setup	26
Supplementary Figure 20. A thermographic image of a patterned ITO glass slide with a bolometric camera.	27
Supplementary Video 1. Thermographic video.	27
Supplementary Video 2. Thermographic video and corresponding histogram.	27
Supplementary Figure 21. Histogram of pixel-to-pixel temperature variation in a still image	28
Supplementary Table 4. Comparison of specifications for thermography methods	28
Supplementary References	29



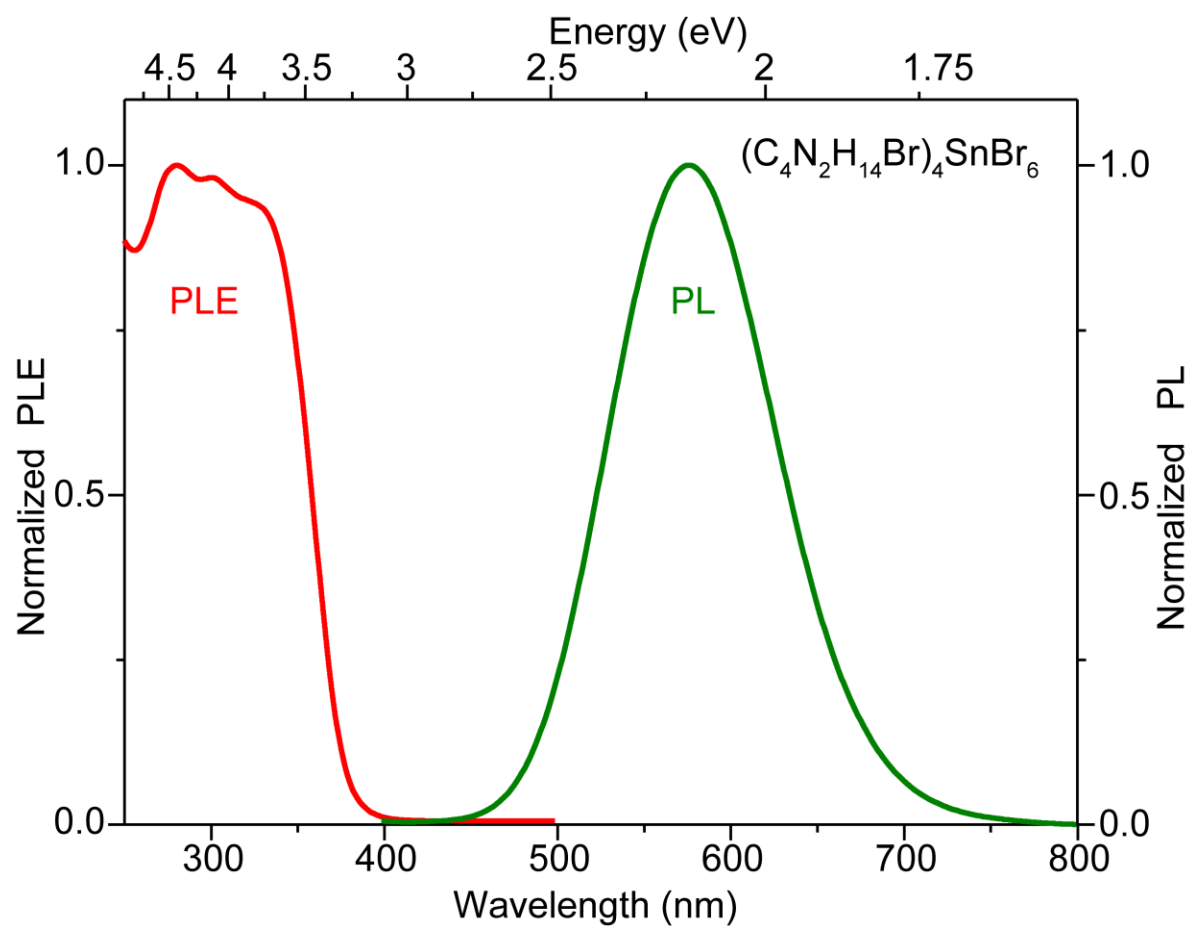
Supplementary Figure 1. Powder X-ray diffraction pattern of Cs_4SnBr_6 .



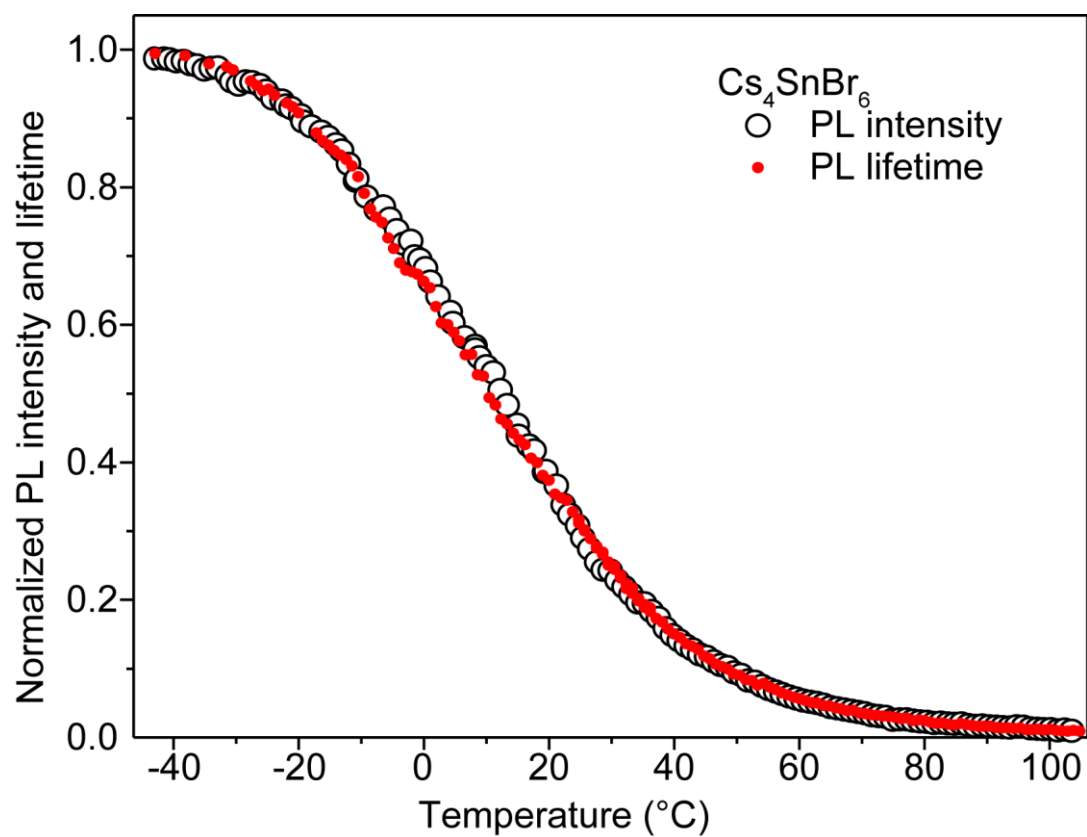
Supplementary Figure 2. Powder X-ray diffraction pattern of $[\text{C}(\text{NH}_2)_3]_2\text{SnBr}_4$.



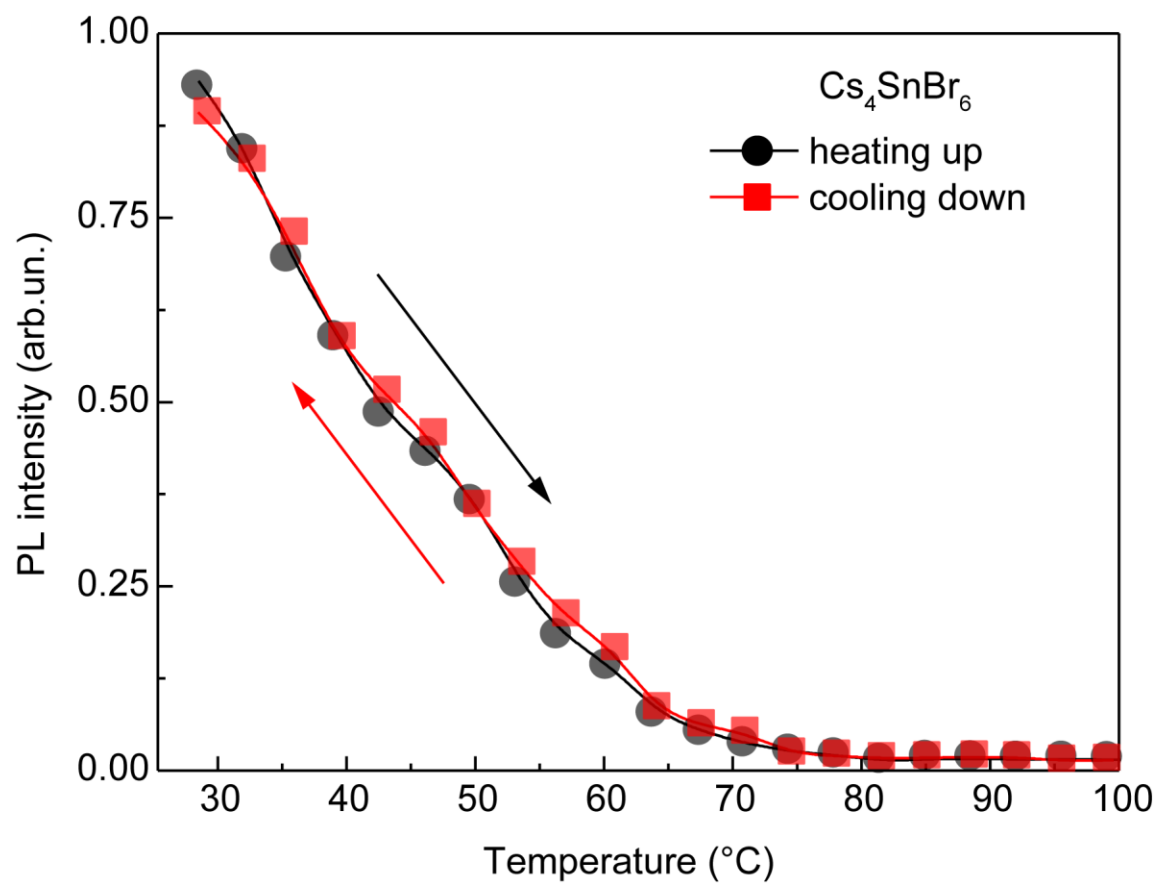
Supplementary Figure 3. Powder X-ray diffraction pattern of $(\text{C}_4\text{H}_{14}\text{N}_2\text{I})_4\text{SnI}_6$.



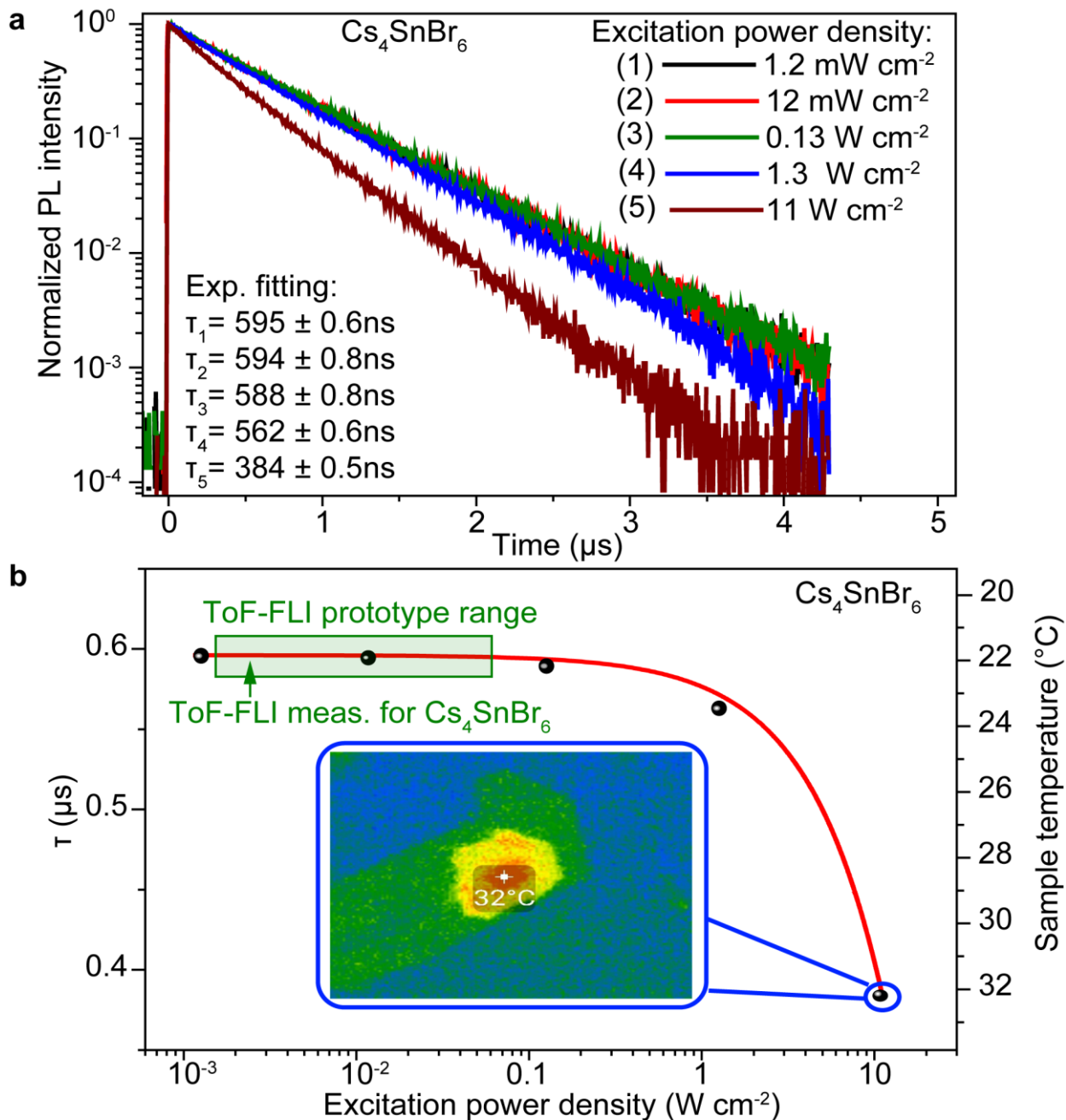
Supplementary Figure 4. Optical characterization of $(\text{C}_4\text{N}_2\text{H}_{14}\text{Br})_4\text{SnBr}_6$: photoluminescence excitation (PLE, red) and photoluminescence (PL, green) spectra.



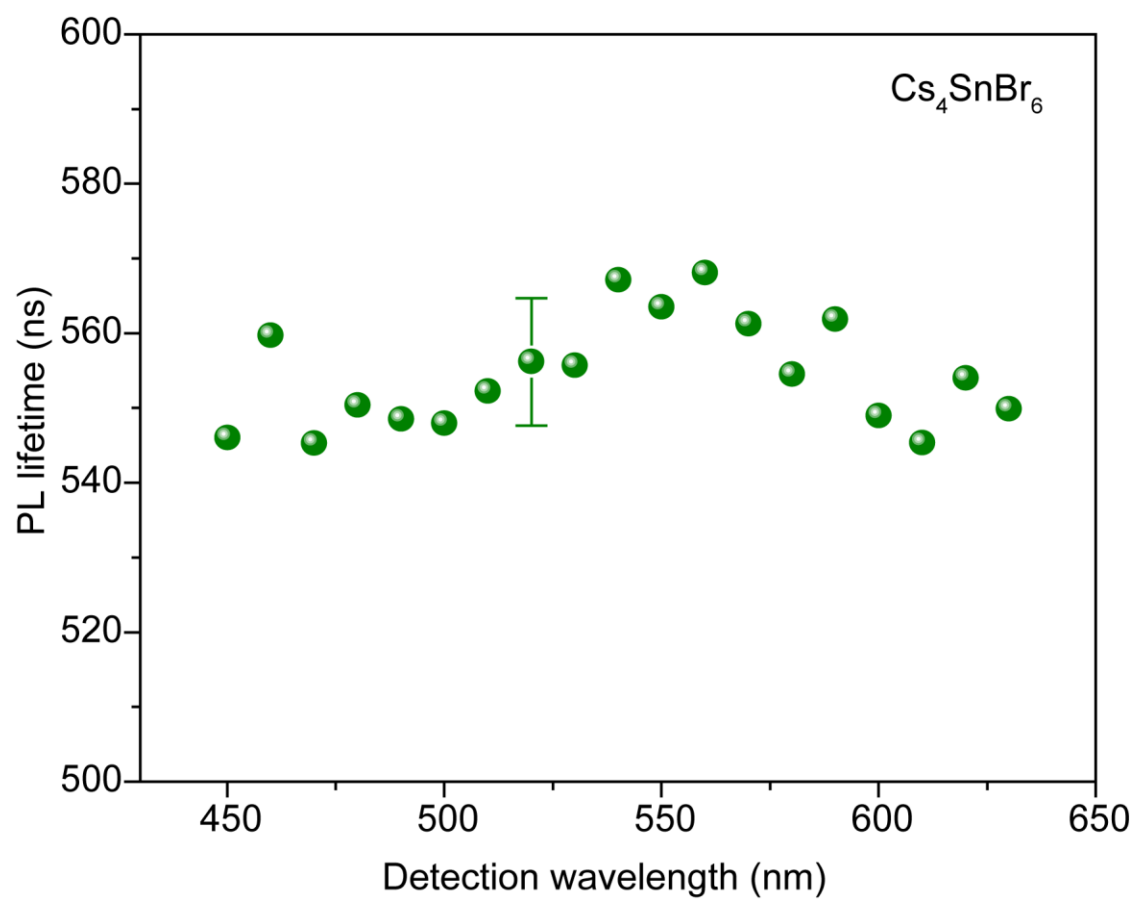
Supplementary Figure 5. Temperature dependence of Cs_4SnBr_6 PL emission lifetime and intensity.



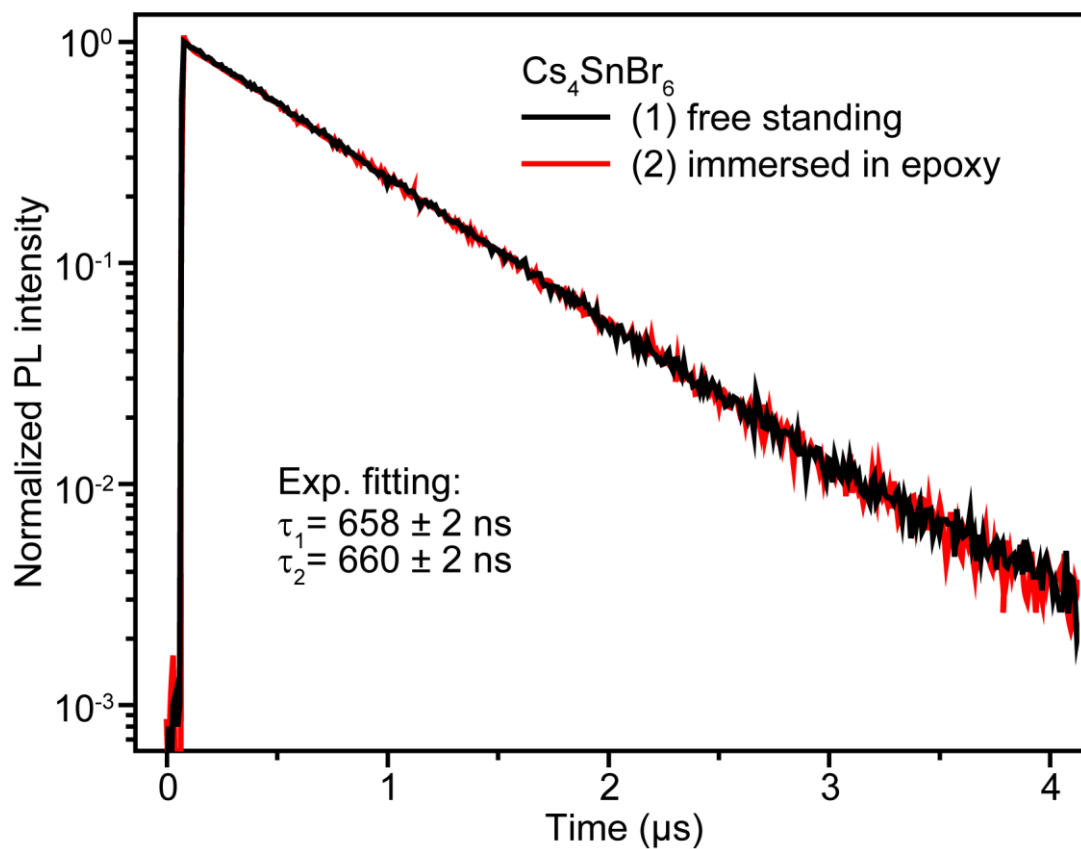
Supplementary Figure 6. Reversible thermal quenching for Cs_4SnBr_6 PL emission.



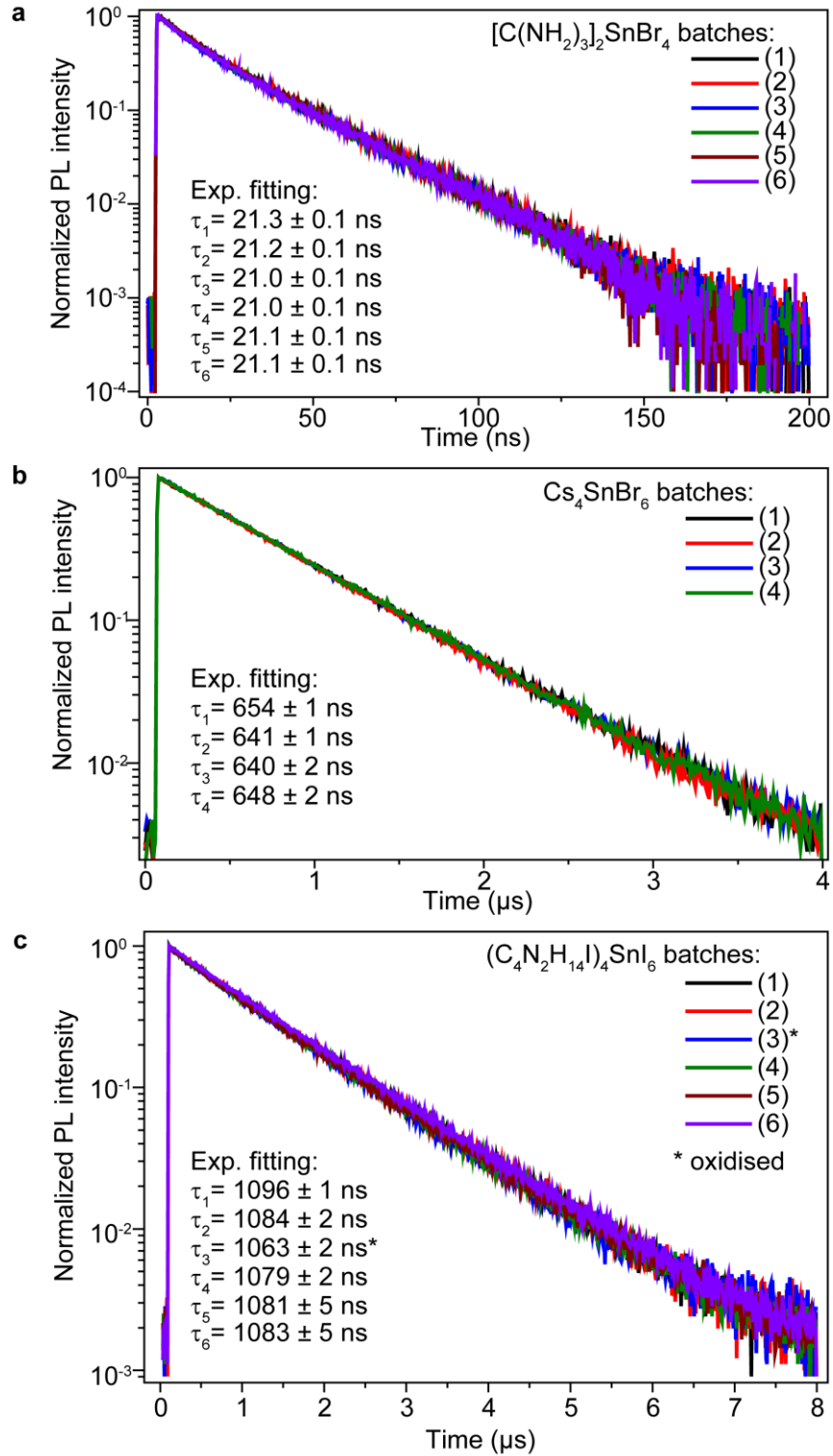
Supplementary Figure 7. Excitation induced heating effects (a) Time-resolved PL traces for Cs_4SnBr_6 at different excitation power densities. (b) Corresponding lifetime values. Inset shows a thermogram captured with a bolometric camera depicting the excitation-induced heating effect for a sample under 11 W cm^{-2} laser excitation. The green arrow depicts the level of excitation power density used in the measurements shown in Figure 3d, Supplementary Figure 21, and Supplementary Videos 1,2; the green rectangle shows the intensity range for the ToF-FLI setup.



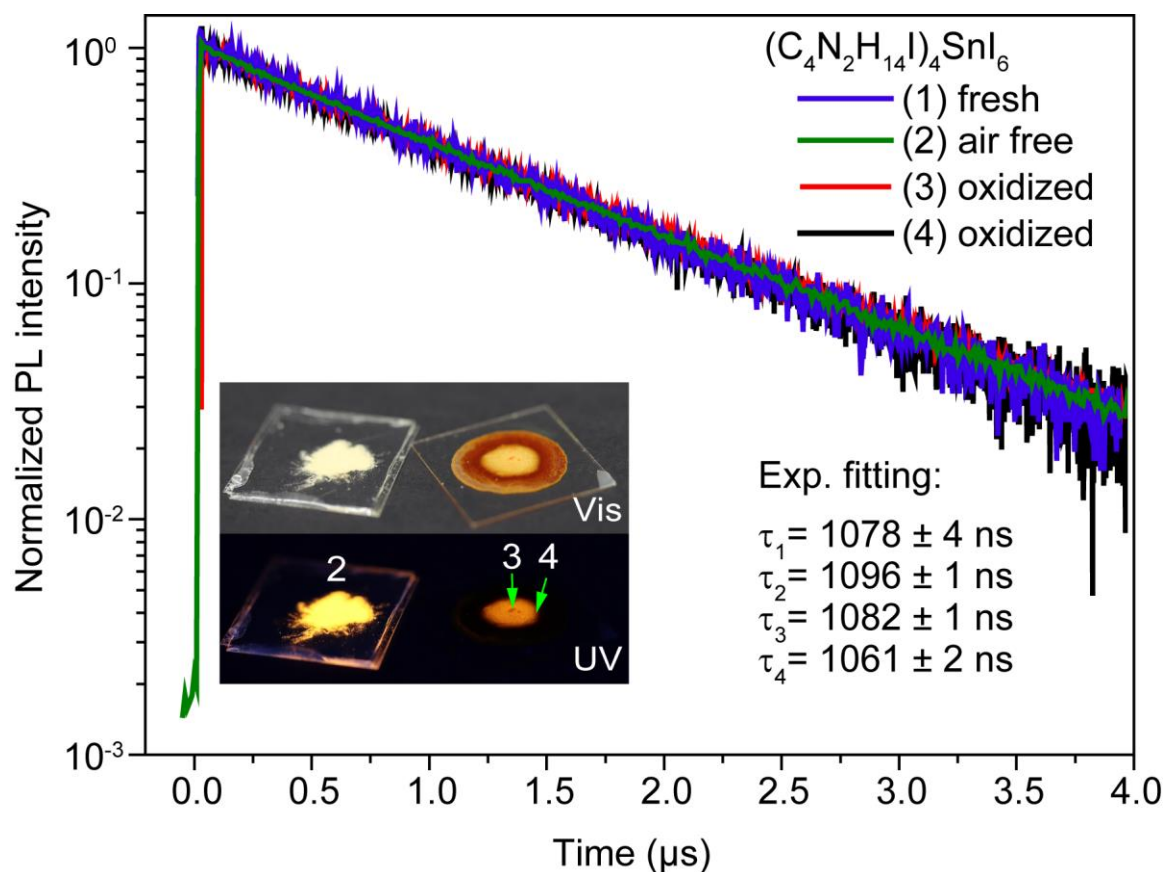
Supplementary Figure 8. Spectrally resolved PL emission lifetimes for Cs_4SnBr_6 .



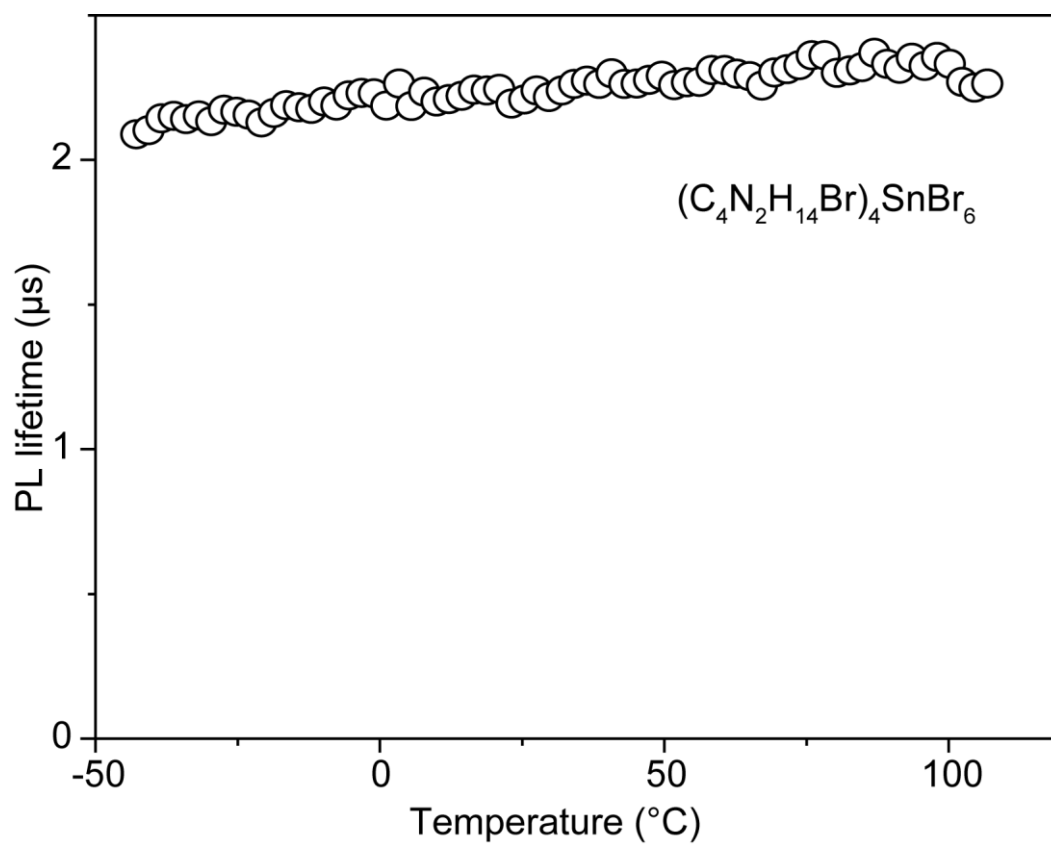
Supplementary Figure 9. Effect of surrounding on time-resolved PL traces for Cs_4SnBr_6 .



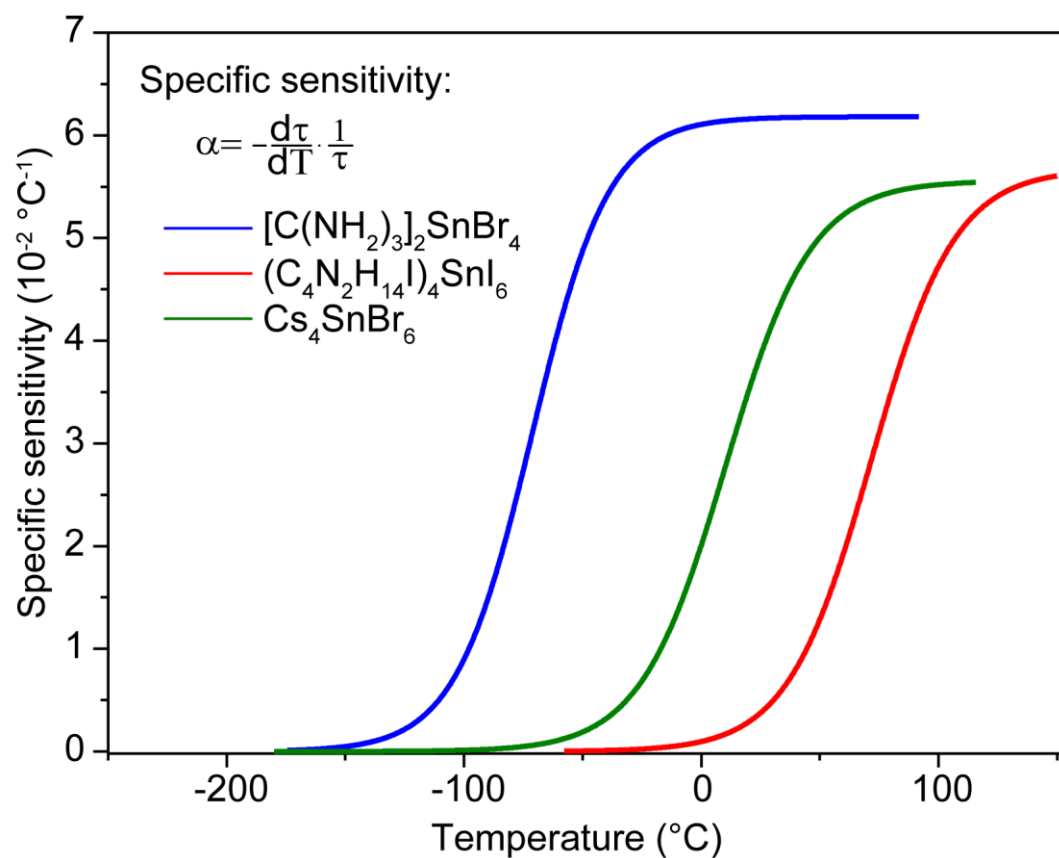
Supplementary Figure 10. Time-resolved PL traces for several batches of (a) $[\text{C}(\text{NH}_2)_3]_2\text{SnBr}_4$, (b) Cs_4SnBr_6 , (c) $(\text{C}_4\text{N}_2\text{H}_{14}\text{I})_4\text{SnI}_6$. Measured lifetimes vary mostly as a result of room temperature fluctuation.



Supplementary Figure 11. Invariance of PL lifetime of $(\text{C}_4\text{N}_2\text{H}_{14}\text{I})_4\text{SnI}_6$ on oxidation and long-term (about 1-year) storage. Inset shows the corresponding non-oxidized (2) and oxidized (various levels of oxidation with point 3 having less and point 4 having more) samples under ambient and UV illumination. Trace 1 depicts the PL lifetime from the as-synthesized $(\text{C}_4\text{N}_2\text{H}_{14}\text{I})_4\text{SnI}_6$ sample. Measured lifetimes vary mostly as a result of room temperature fluctuation.



Supplementary Figure 12. PL lifetime temperature dependence for $(\text{C}_4\text{N}_2\text{H}_{14}\text{Br})_4\text{SnBr}_6$.



Supplementary Figure 13. Specific sensitivity. The dependence of specific sensitivity on temperature for [C(NH₂)₃]₂SnBr₄ (blue), Cs₄SnBr₆ (green), (C₄N₂H₁₄I)₄SnI₆ (red).

Supplementary Note 1. Models for the fitting of PL lifetime vs. temperature dependence.

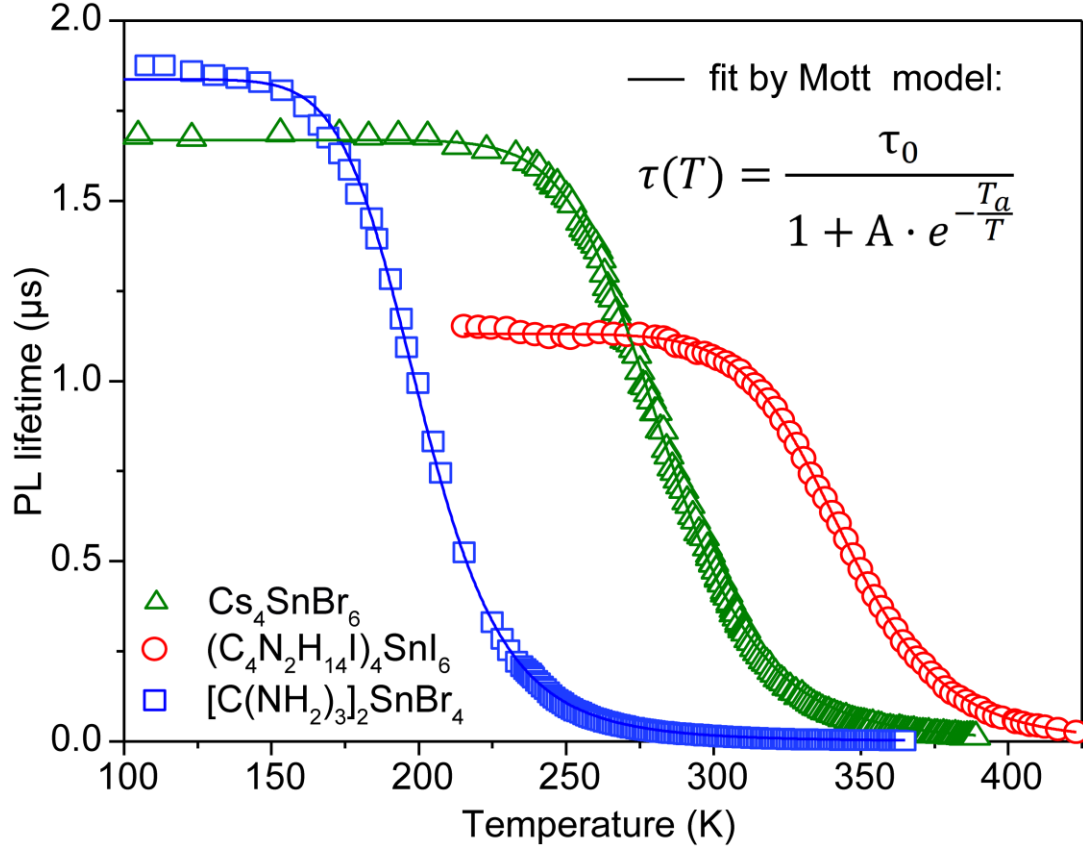
In order to understand the nature of the thermal quenching of emission and the lifetime acceleration in tin-halide luminophores, we fit temperature dependent PL-lifetime data with several suitable models (Figs.S13-S15; Table S1-3). With the first model, we suggested a thermal activation process according to the Mott model, $\tau(T) = \frac{\tau_0}{1+A \cdot e^{-\frac{T_a}{T}}}$, where τ_0 is the intrinsic radiative lifetime, A is a pre-exponential factor (in which $\frac{A}{\tau_0}$ is the non-radiative rate), T_a is the activation temperature, and T is the temperature in K. Although the model agrees with the experimental data, we found that it is difficult to provide a physical interpretation for the fitting parameters: A and T_a , which are exceedingly large (10^7 and 6000 K, respectively; Fig. S13, Table S1).

Next, we chose the Boltzmann-sigmoid model, which also provided a proper fit for the experimental data according to the equation: $\tau(T) = \frac{\tau_0}{1+e^{\frac{T-T_B}{\Delta T}}}$ where τ_0 is the intrinsic radiative lifetime, T_B and ΔT are respectively the center and half-width of the temperature sensitive range, and T is the temperature in K (Fig.S14). Despite the fact that the fitting parameters in this model (Table S2) do indeed yield realistic values, the model itself cannot be attributed to any physical quenching process.

Therefore, as a compromise between simplicity and the ability to realistically interpret the model, we chose the exciton-phonon scattering model: $\frac{1}{\tau(T)} = \frac{1}{\tau_0} + \frac{\Gamma_{ph}}{\left(e^{\frac{E_{ph}}{kT}} - 1\right)^m}$, where τ_0 is the intrinsic radiative lifetime, Γ_{ph} is the exciton-phonon scattering probability, E_{ph} is the phonon energy, m is the number of phonons, k is the Boltzmann constant, and T is the temperature in K (Fig. S15, Table S3).¹

This model succeeds in providing phonon energies that can be converted to physically relevant activation temperatures (Table S3, column where E_{ph} is shown in units of K). Furthermore, these

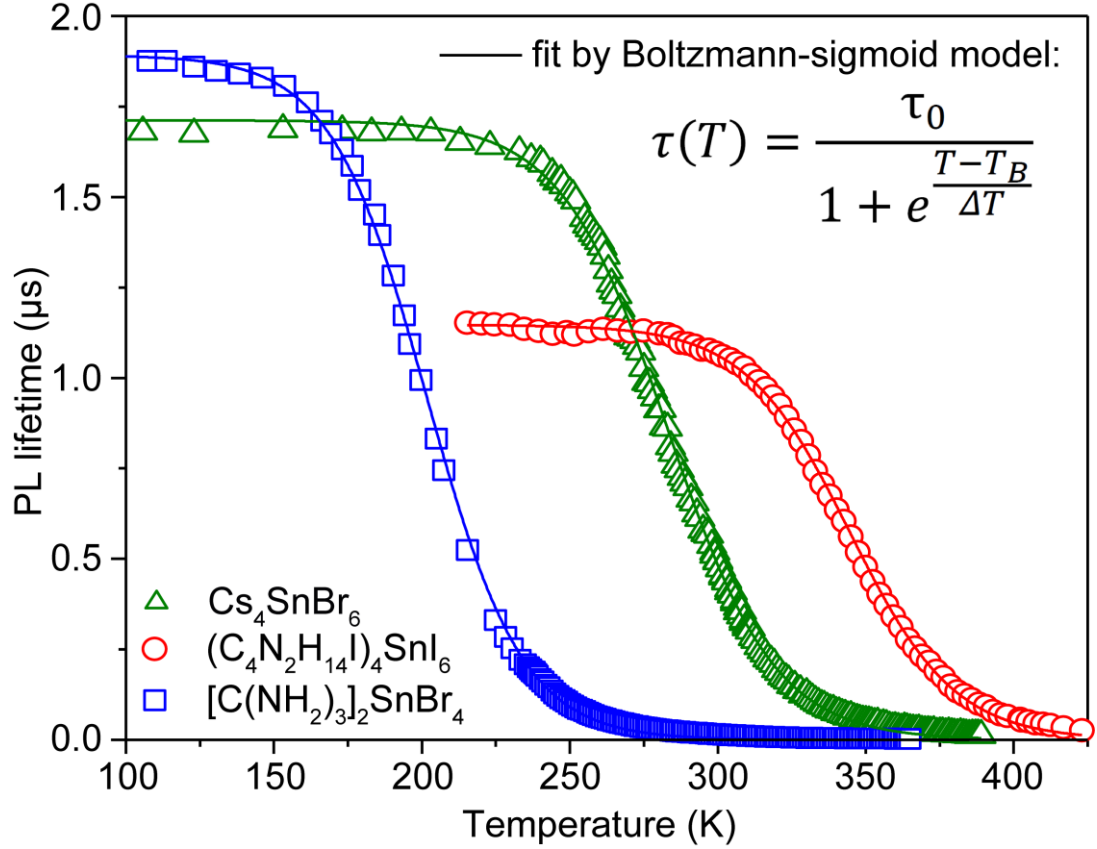
temperatures agree extremely well with the observed onset of lifetime acceleration in each case. This model, however, predicts a rather high number of phonons involved in the scattering process ($m \sim 10$). Such high values of m might be explained through collective processes that involve high numbers of phonons, but this is also unrealistic given the low probability of such an event occurring. It is possible that there exists an essentially nonlinear temperature dependence in the phonon-exciton interaction, and the self-trapped excitons within such systems require another model to provide a satisfactory description of their thermal behavior.



Supplementary Figure 14. Fitting by the Mott model. PL lifetime temperature dependence for $[\text{C}(\text{NH}_2)_3]_2\text{SnBr}_4$ (blue squares), Cs_4SnBr_6 (green triangles), $(\text{C}_4\text{N}_2\text{H}_{14}\text{I})_4\text{SnI}_6$ (red circles) by fitting with an Mott model (colored lines): $\tau(T) = \frac{\tau_0}{1 + A \cdot e^{-\frac{T_a}{T}}}$.

Supplementary Table 1. Fitting parameters for the Mott model.

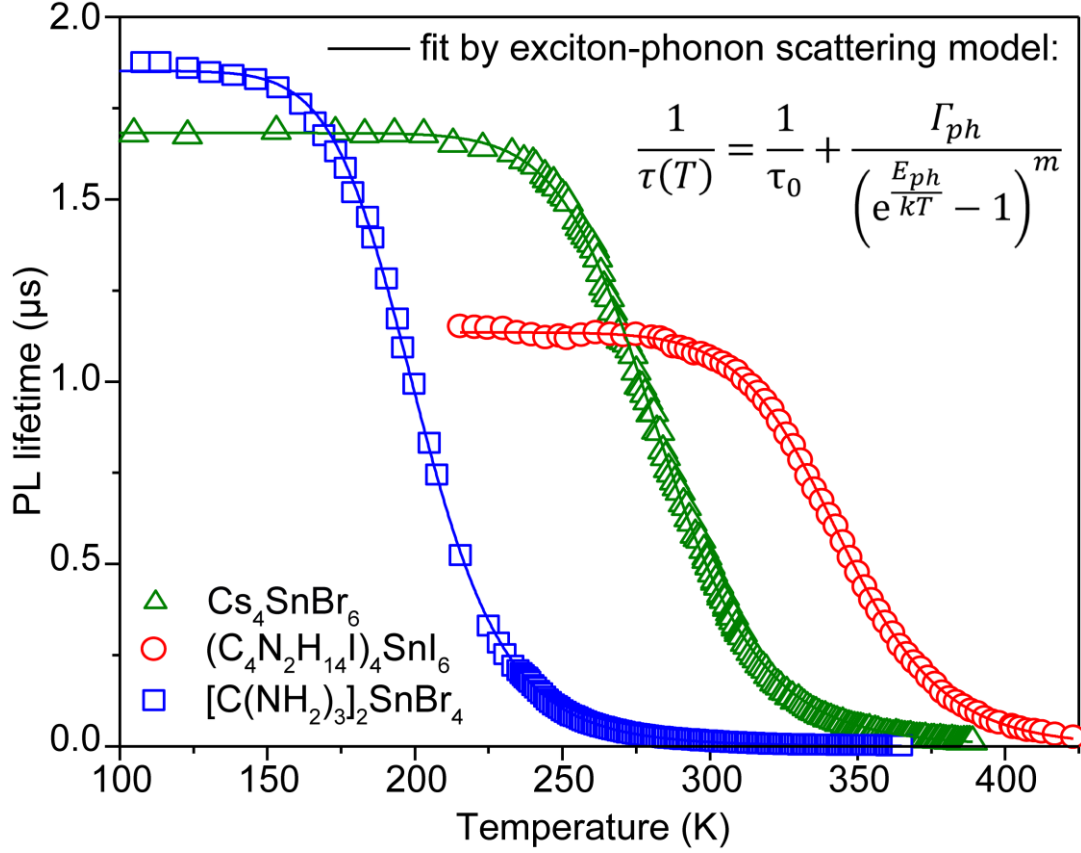
Composition	τ_0	A	T_a	E_a	Temperature sensitivity range
	ns		K	eV	°C (K)
Cs_4SnBr_6	1669	$1.9 \cdot 10^7$	4759	0.41	-30 – 40 (243 - 323)
$[\text{C}(\text{NH}_2)_3]_2\text{SnBr}_4$	1837	$1.5 \cdot 10^6$	2863	0.25	-100 – 30 (173 - 243)
$(\text{C}_4\text{N}_2\text{H}_{14}\text{I})_4\text{SnI}_6$	1131	$5.7 \cdot 10^8$	6945	0.6	40 – 110 (313 - 383)



Supplementary Figure 15. Fitting by the Boltzmann-sigmoid model. PL lifetime temperature dependence for $[\text{C}(\text{NH}_2)_3]_2\text{SnBr}_4$ (blue squares), Cs_4SnBr_6 (green triangles), $(\text{C}_4\text{N}_2\text{H}_{14}\text{I})_4\text{SnI}_6$ (red circles) by fitting with the Boltzmann-sigmoid model (colored lines): $\tau(T) = \frac{\tau_0}{1 + e^{\frac{T-T_B}{\Delta T}}}$.

Supplementary Table 2. Fitting parameters for Boltzmann-sigmoid model. Temperature sensitivity ranges are determined as $T_B \pm 2\Delta T$.

Composition	τ_0	T_B	ΔT	Temperature sensitivity range	E_{ph}
	ns	K	K		meV
Cs_4SnBr_6	1711	281	18	-30 – 40 (243 - 323)	24
$[\text{C}(\text{NH}_2)_3]_2\text{SnBr}_4$	1892	205	17	-100 – -30 (173 - 243)	18
$(\text{C}_4\text{N}_2\text{H}_{14}\text{I})_4\text{SnI}_6$	1146	345	18	40 – 110 (313 - 383)	30



Supplementary Figure 16. Fitting by the exciton-phonon scattering model. PL lifetime temperature dependence for $[\text{C}(\text{NH}_2)_3]_2\text{SnBr}_4$ (blue squares), Cs_4SnBr_6 (green triangles), $(\text{C}_4\text{N}_2\text{H}_{14}\text{I})_4\text{SnI}_6$ (red circles) by fitting with the exciton-phonon scattering model (colored lines): $\frac{1}{\tau(T)} = \frac{1}{\tau_0} + \frac{\Gamma_{ph}}{\left(\frac{E_{ph}}{e kT} - 1\right)^m}$.

Supplementary Table 3. Fitting parameters for the exciton-phonon scattering model.

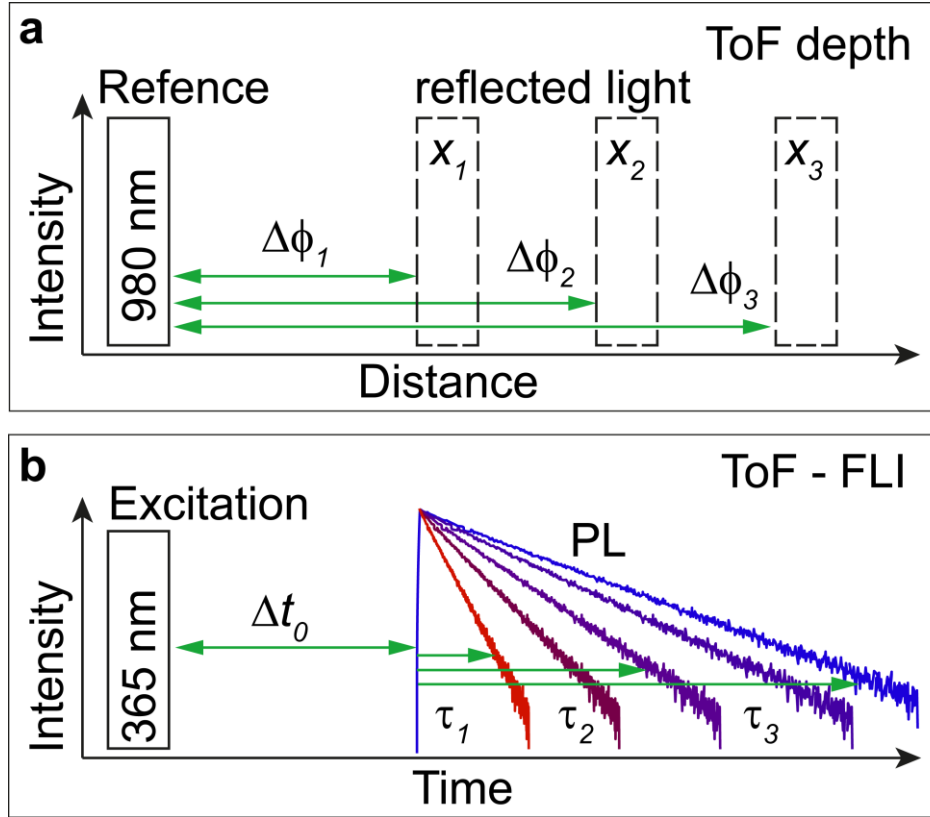
Composition	τ_0	Γ_{ph}	E_{ph}		m	Temperature sensitivity range
	ns	10^{-6} s^{-1}	meV	K		$^{\circ}\text{C}$ (K)
Cs_4SnBr_6	1681	0.053	21.3	247	10.7	-30 – 40 (243 - 323)
$[\text{C}(\text{NH}_2)_3]_2\text{SnBr}_4$	1851	0.03	15.6	181	8.7	-100 – -30 (173 - 243)
$(\text{C}_4\text{N}_2\text{H}_{14}\text{I})_4\text{SnI}_6$	1135	0.13	25.2	292	13	40 – 110 (313 - 383)



Supplementary Figure 17. Photographs of the depth standard for ToF imaging in Fig.4a.

Supplementary Note 2. Basic principles of ToF-FLI.

Depth images such as those produced by the ToF sensor in the Kinect 2.0 from Microsoft Corp. are measured by the phase shift $\Delta\phi$ (equivalent to the delay time) of the reflected light relative to the IR reference beam due to light propagation x (Supplementary Fig.S17a). For the depth imaging we take into account the fact that the reflection is an immediate process on the contrary to PL that has an intrinsic delay associated with the PL lifetime. The ToF-measurement of the delay caused by the luminophore's PL lifetime τ makes the use of ToF-FLI possible (Supplementary Fig.S17b). To do so, we switched to UV excitation (as an analog to the IR reference beam used in the Kinect 2.0) and rejected any scattered or reflected UV light by optical cut-off filters to exclusively record the PL delay. However, an additional reference measurement without optical filters (to register UV light reflected by the sample) is required to determine the initial delay time Δt_0 . This delay time occurs as a result of the optical path of the measurement scheme as well as variations which result from inhomogeneities in a sample's topography. This must be correctly accounted for to precisely determine the PL lifetime, τ .



Supplementary Figure 18. Scheme describing optical ToF measurements. (a) The estimation of distance x by the measured phase shift $\Delta\phi$. (b) Similar ToF hardware principles apply to the estimation of PL decay.

Supplementary Note 3. Frequency domain PL lifetime measurement by phase-shift.

ToF-FLI is based on a mathematical model where the observed PL emission trace is shown as a convolution of a harmonically modulated excitation signal with a mono-exponential emission relaxation decay:

$$I_{PL}(t) = \int_0^t B \cdot (1 + \cos(2\pi\nu x + \frac{\pi}{2})) \cdot e^{-\frac{t-x}{\tau}} dx, \quad (1)$$

where B is a scaling coefficient, ν is the excitation modulation frequency, and τ is an exponential decay parameter. The result of convolution (1) is a harmonically oscillating trace that has a certain phase delay ϕ from the excitation trace (Fig.4b). In the case of a mono-exponential decay the result of the phase delay is determined² by:

$$\tau = \frac{\tan(\Delta\phi)}{2\pi\nu} \quad (2)$$

The working principle for a ToF image sensor is based on the acquisition of four, phase-locked images at 0°, 90°, 180° and 270° phase delay with respect to the excitation signal (I_0 , I_1 , I_2 and I_3 on Fig.4b).³ From these four images, the spatial distribution of the PL intensity I , modulation index M , and phase angle $\Delta\phi$ can be computed:

$$\Delta\phi = \arctan\left(\frac{I_0 - I_2}{I_3 - I_1}\right) \quad (3)$$

$$M = 2 \frac{\sqrt{(I_1 - I_3)^2 - (I_0 - I_2)^2}}{I_0 + I_1 + I_2 + I_3} \quad (4)$$

$$I = \frac{I_0 + I_1 + I_2 + I_3}{4} \quad (5)$$

The lifetime is then calculated using Eq. (2). In the ToF-FLI prototype used in this study (Fig. S18), each pixel of the imaging chip is capable of performing this measurement in parallel, thus circumventing the need for bulky and expensive scanning systems.

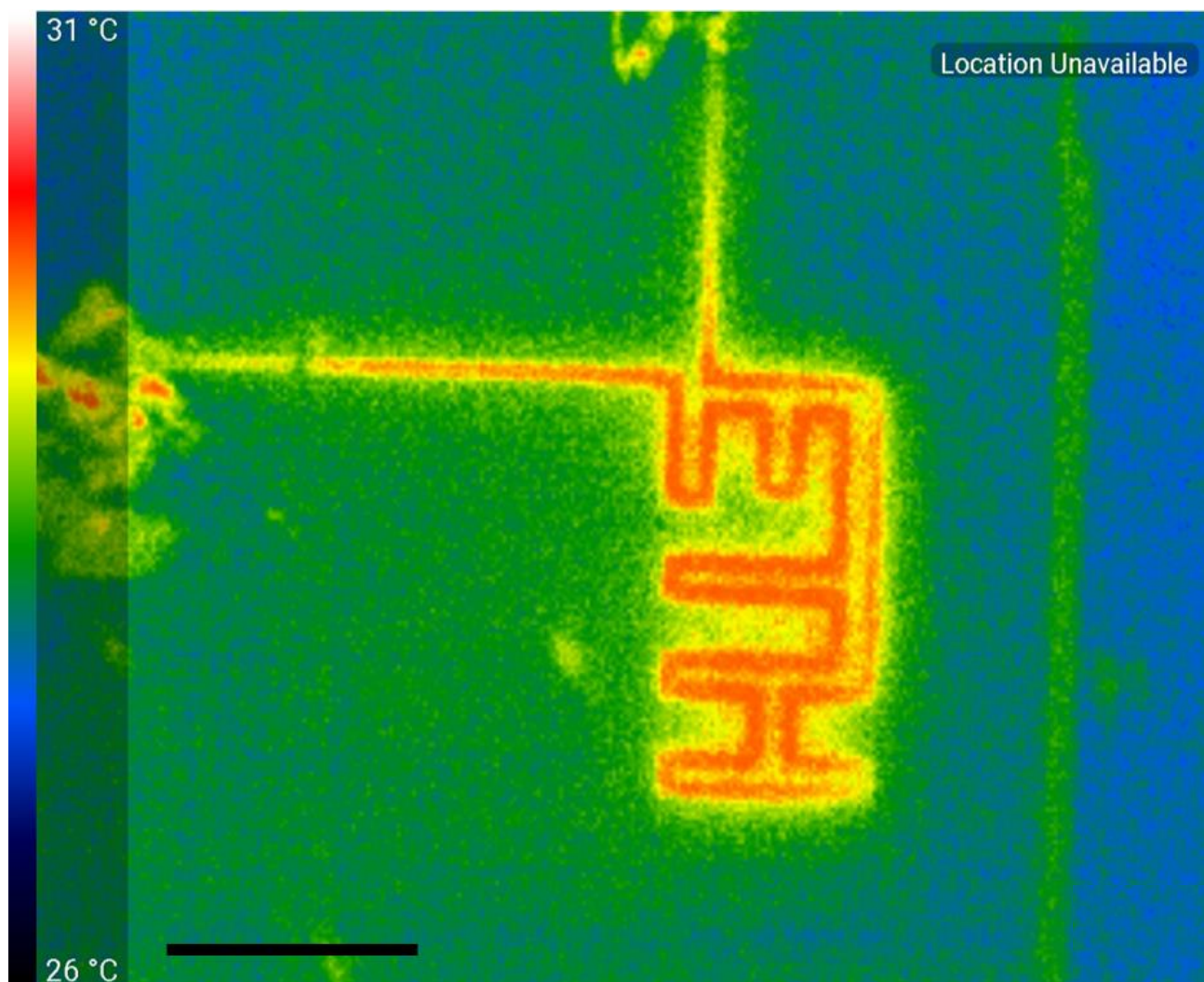


Supplementary Figure 19. Compact stand-alone ToF-FLI prototype developed by CSEM (Switzerland) for real-time, wide-field fluorescence lifetime imaging in the nano- to micro-second range. Scale bar is 5 cm.

Supplementary Note 4. Key specifications of ToF-FLI image sensor used in the setup:

- Number of pixels: 256 x 256 pixels
- Maximum frame rate at full resolution: 100 fps
- Analog outputs (no on-chip ADC)
- Pixel size: 6.3 x 6.3 μm \rightarrow Active area size 1.6 mm x 1.6 mm
- Maximum demodulation frequency: 4 x 20 MHz = 80 MHz
- Quantum efficiency (QE): 0.43@600nm, 0.21@800nm, 0.14@850nm
- Fill factor: 14 %
- Dark current: 40 e-
- Pixel saturation capacitance: 9 ke-
- Maximum SNR: 39.9 dB
- Dynamic range: 49.9 dB

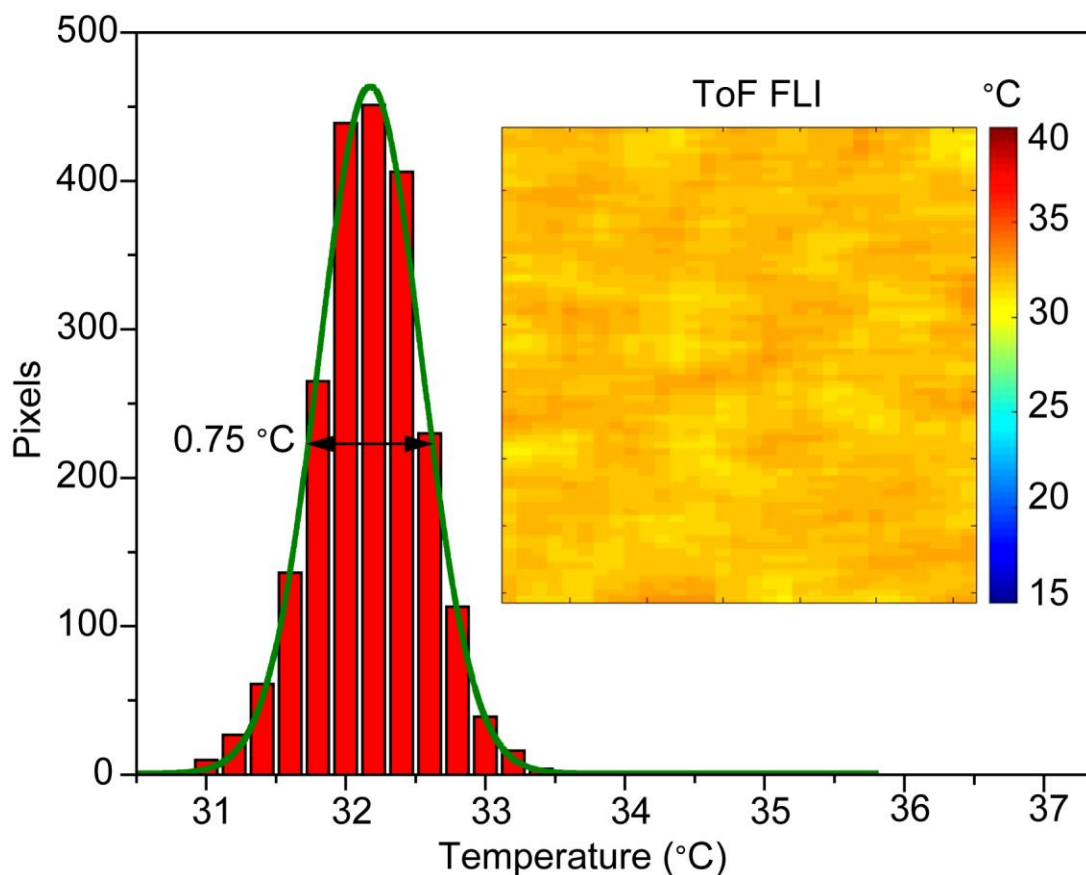
Detailed description of image sensor architecture can be found in Supplementary Ref. ⁴.



Supplementary Figure 20. A thermographic image of a patterned ITO glass slide with a bolometric camera. The sample was heated with a passing electrical current, and acquired with a commercial LWIR bolometry camera equipped with a ZnSe lensed macro-objective. Scale bar is 3 mm.

Supplementary Video 1. Thermographic video. The dynamics of temperature change in the sample and heat transfer through the substrates due to brief contact with a hot soldering pin (the temperature of pin apex was approx. 120 °C). The sample is $(\text{C}_4\text{N}_2\text{H}_{14}\text{I})_4\text{SnI}_6$ powder encapsulated between two relatively thick (1mm) glass substrates.

Supplementary Video 2. Thermographic video and corresponding histogram. Dynamic histogram showing the pixel-to-pixel temperature variation in a ToF-FLI thermographic video recorded for homogeneously heated sample of Cs_4SnBr_6 .



Supplementary Figure 21. Histogram of pixel-to-pixel temperature variation in a still image (shown in the inset) taken from a ToF-FLI thermographic video recorded for a homogeneously heated sample of Cs_4SnBr_6 . The evaluated image area contains roughly 2200 pixels.

Supplementary Table 4. Comparison of specifications for thermography methods.

	TCSPC	ToF	IR@ RT, bolometers
Exc. power density	0.01-100 mW cm ⁻²	~60 mW cm ⁻²	NA
Frame rate	~0.1 min ⁻¹	3-100 s ⁻¹	6-60 s ⁻¹
Distance	10 ⁻² -100 m	10 ⁻² -3 m	10 ⁻¹ -100 m
Meas. Prec.	15 mK	~1 K	0.1-1 K

Supplementary References

1. Man, M. T. & Lee, H. S. and carrier-phonon scattering in quantum dot population dynamics. *Sci. Rep.* **5**, 8267, (2015).
2. Hansard, M., Lee, S., Choi, O. & Huraud, R. *Time-of-Flight Cameras: Principles, Methods and Applications*. (Springer Publishing Company, Incorporated, 2012).
3. Foix, S., Alenya, G. & Torras, C. Lock-in Time-of-Flight (ToF) Cameras: A Survey. *IEEE Sens. J.* **11**, 1917-1926, (2011).
4. Bonjour, L. E., Singh, A., Baechler, T. & Kayal, M. in *2011 IEEE SENSORS Proceedings*. 724-727 (IEEE).